crystals

MDPI

Article

Computational Study on Homogeneous Melting of Benzene Phase I

Kenji Mochizuki [1,2]

[1] Institute for Fiber Engineering, Shinshu University, Ueda, Nagano 386-8567, Japan; mochizuki@shinshu-u.ac.jp

[2] Department of Chemistry and Materials, Faculty of Textile Science and Technology, Ueda, Nagano 386-8567, Japan

Received: 18 January 2019; Accepted: 3 February 2019; Published: 5 February 2019



Abstract: Molecular-dynamics simulations are used for examining the microscopic details of the homogeneous melting of benzene phase I. The equilibrium melting temperatures of our model were initially determined using the direct-coexistence method. Homogeneous melting at a higher temperature is achieved by heating a defect- and surfacefree crystal. The temperature-dependent potential energy and lattice parameters do not indicate a premelting phase even under superheated conditions. Further, statistical analyses using induction times computed from 200 melting trajectories were conducted, denoting that the homogeneous melting of benzene occurs stochastically, and that there is no intermediate transient state between the crystal and liquid phases. Additionally, the critical nucleus size is estimated using the seeding approach, along with the local bond order parameter. We found that the large diffusive motion arising from defect migration or neighbor-molecule swapping is of little importance during nucleation. Instead, the orientational disorder activated using the flipping motion of the benzene plane results in the melting nucleus.

Keywords: benzene; phase transition; melting; homogeneous nucleation; critical nucleus; plastic phase; molecular dynamics

1. Introduction

Melting is of fundamental importance in science because of interest in the manner in which crystalline solids spontaneously lose their energetically favored order [1,2]. In nature, melting is usually initiated heterogeneously on surfaces, and a solid material immediately transforms into a liquid that is maintained at higher than the material's melting temperature [3,4]. However, melting homogeneously occurs inside a crystal if surface melting is suppressed, which can be experimentally achieved using coating [5,6] or laser [7–12] techniques. Homogeneous melting can be defined as the phase transition from solid to liquid in the surface- and defectfree crystal, in which there is no trigger to initiate disordering except thermal fluctuations, and nucleation is equally likely to occur anywhere.

In an earlier study, the limit of superheating was predicted using two different parameters based on vibrational instability and elastic shear instability, the Lindemann [1] and Born criteria [2], respectively. Even though experimental observation of the initial stage of homogeneous melting remains challenging because of the random creation of a liquid nucleus and its subsequent fast growth [5–13], recent developments in computer simulation have enabled us to closely examine its microscopic details [14–27]. Using molecular-dynamics (MD) simulations for a Lennard–Jones fluid, a study by Jin et al. observed that homogeneous melting is initiated by clusters of vibrationally destabilised particles by satisfying the Lindemann and Born criteria [16,28]. Although other computational studies of various materials have demonstrated homogeneous melting via nucleation, a considerable diversity of defects or precursors that trigger melting can be observed, including

a complex multiscale pathway involving point defects and dislocations [17], topological defects [18,19], separation [20] or aggregation [21,22] of interstitial-vacancy (Frenkel) pairs, and stringlike [23–26] as well as looplike [27] co-operative motions.

Benzene is a renowned hexagonal, small, and simple molecule. Regardless, its polymorphism [29–31] and local liquid structure [32–34] have not been completely explored. Although benzene's phase-transition dynamics have briefly been investigated [35–37], interesting phase behavior may be observed in the melting process. In 1982, Tohji et al. examined the lattice parameters of benzene phase I (stable phase under ambient pressure) via powder X-ray diffraction, and claimed the existence of a premelting stage that can be observed at 10 K below melting point [36]. Furthermore, they predicted that the orientational disorder phase, plastic crystal, appears as a transient state during the transition process from the crystal phase to the liquid phase. The premelting effect was later considered to be disproven after an investigation over the complete temperature range of 4–280 K [37]. However, the molecular mechanism of the melting dynamics of benzene, including the possibility of occurrence of a transient plastic phase, has not yet been clarified.

In the current study, we perform MD simulations for examining the molecular mechanism of the homogeneous melting of benzene phase I. We determine the equilibrium melting temperatures by implementing the direct-coexistence method and the homogeneous-melting temperature by heating up a surfacefree crystal. Further, we perform statistical analyses of induction times to investigate which of linear or stepwise transition is dominant in benzene melting. We used the seeding approach with the local bond order parameter for estimating critical nucleus size. Finally, we examine the key molecular motion that is required to form the critical melting nucleus.

2. Methods

2.1. Model

The benzene molecule was modelled with full atomistic detail using CHARMM22 [38,39]. Van Der Waals energy is calculated with a standard 12-6 Lennard–Jones potential and the electrostatic energy with a Coulombic potential. It was demonstrated that this force field reproduces the crystal structure of benzene phase I [35,40]. Other studies have also claimed that partial charges affect the orientation of benzene dimer [41] and the phase diagram for the other polycyclic aromatic hydrocarbons [42]. Intermolecular interactions are truncated at 1.20 nm. The Lennard–Jones parameters of cross-interactions are obtained using the Lorentz–Berthelot combination rules: $\epsilon_{ij} = (\epsilon_{ii} \cdot \epsilon_{jj})^{1/2}$ and $\sigma_{ij} = (\sigma_{ii} + \sigma_{jj})/2$. Long-range Coulombic interactions are evaluated using the particle-mesh Ewald algorithm [43].

2.2. Molecular-Dynamics Simulation

MD simulations were conducted using the GROMACS 2018.3 package [44], where equations of motion are integrated with the leapfrog algorithm using a time step of 2 fs. Temperature T for production runs is controlled using the Nosé–Hoover thermostat [45,46] with damping constants of 1.0 ps, while the Berendsen algorithm [47] is used for equilibration. Pressure p is anisotropically controlled using the Berendsen algorithm [47] with damping constants of 2.0 ps, and pressurewasis set to 1.0 atm in all simulations. Energy minimization was conducted using the steepest-descent method. Periodic boundary conditions were applied in all three directions.

To determine the homogeneous melting temperature, we heated the system at 10 K intervals and performed an NpT-MD run for 10 ns at each T. This heating rate was chosen to observe nucleation after plenty of induction time, and to perform statistical analyses by making two hundred melting trajectories.

2.3. Crystalline Structure

The structure of the benzene phase I crystal unit cell was obtained from the Cambridge Structural Database (refcode: BENZEN, Deposition Number: 1108749) [48]. The orthorhombic unit cell contains four benzene molecules, and the space group is *Pbca*. Further, lattice parameters are $a = 7.460$, $b = 9.666$, and $c = 7.034$ Å at 270 K [49]. Each benzene molecules has 12 neighbors, and their centers of mass are arranged in a pseudo-face-centred cubic (pseudo-FCC) lattice. We replicated the unit cell in three dimensions to manufacture systems for analyses. In our simulations, lattice axes a, b, and c correspond to the x, y and z axes, respectively.

3. Results and Discussion

3.1. Melting Temperature

We initially evaluated melting temperature T_m of benzene phase I in our model using the direct-coexistence method [50]. We developed two identical boxes of benzene crystal containing 1344 molecules and melted one of them by performing a short NVT-MD simulation at 400 K. Box size was 5.4 × 5.8 × 5.6 nm. We joined these crystal and liquid boxes by erasing the overlapped molecules and making a 5.4 × 12.0 × 5.6 nm rectangular simulation box composed of 2539 molecules, named 'short system' (Figure 1A). We used the periodic boundary condition so that the liquid phase was in contact with the solid on both sides, although we do not show the imaginary cells. To relax the solid–liquid interface, we performed an NVT-MD run for 100 ps by freezing the solid phase, and the subsequent NpT-MD ran for 100 ps without freezing, where both simulations were conducted at 200 K. Further, we performed NpT-MD runs at 260, 265, and 270 K. Figure 1D depicts the time evolution of the average potential energy per molecule for these runs. The liquid has higher potential energy than the solid due to the disordered structure of the liquid, so we used the average potential energy to monitor which of melting or freezing occurs at a given temperature [50,51]. At T_m, the crystal and liquid phases exhibited the same stability in free energy, and their volumes did not change. On the other hand, if $T > T_m$, the volume of liquid increased by the melting of the solid phase, so that the average potential energy increased. In contrast, if $T < T_m$, potential energy decreased. Figure 1D shows that potential energy increased at 265 and 270 K, whereas it decreased at 260 K. These results indicate that 260 K is lower than T_m, while 265 K is higher than T_m, so that T_m is somewhere between 260 and 265 K. Thus, we roughly assume that T_m is 262.5 ± 2.5 K for the short system.

The presence of the interface might complicate the performance of NpT simulations [52]. To assess the accuracy of our estimation for T_m, we performed the same analyses for two other different cell sizes, medium (N = 5078) and long (N = 7617) systems. The initial configurations were prepared in the same manner as for the short system. The system size of medium and long systems was 5.4 × 23.0 × 5.6 nm, and 5.4 × 34.0 × 5.6 nm, respectively. These two systems had the same area of solid–liquid interface as the short system, and length in the direction perpendicular to the interface is two and three times longer, respectively (Figure 1B,C). In other words, these three systems have different size ratios of liquid–solid interface with respect to the whole simulation cell. The time evolution of potential energy for the medium and long systems indicates that T_m is 265 ± 5 K (Figure 1E,F), which error range includes the T_m estimated for the short system. Thus, we suppose that T_m was 265 ± 5 K for our computational model, which is approximately 14 K lower than the experimental estimation of 278.7 K [53].

In a homogeneous regime, crystal structure can be superheated to a metastable state; its actual melting temperature is considerably higher than equilibrium melting temperature T_m [5,10,15,20,50]. To determine homogeneous melting temperature, we made a crystal structure of N = 7280, with a box size of 9.6 × 9.4 × 9.5 nm, and equilibrated the system at 240 K. Then, we heated the system in increments of 10 K, performing an NpT-MD simulation for 10 ns at each T. We observed that melting occurs at 330 K as soon as T is increased from 320 K. Figure 2A depicts that the average potential energy per molecule jumps between T = 320 and 330 K owing to the first-order phase transition, whereas it continuously increases at other temperatures. This result indicates that the limit of superheating

achieved by our heating rate (1.0 K/ns) is 330 K, which is approximately 70 K higher than T_m. Furthermore, we confirmed that the lattice parameters of the crystal (a, b, and c) change continuously at lower than 320 K (Figure 2B). Craven et al. demonstrated the smooth variation of the lattice parameters below T_m using neutron-powder diffraction [37]. In our result, smooth variation was observed until 320 K. Thus, we could conclude there was no hint of premelting, even for a superheated condition.

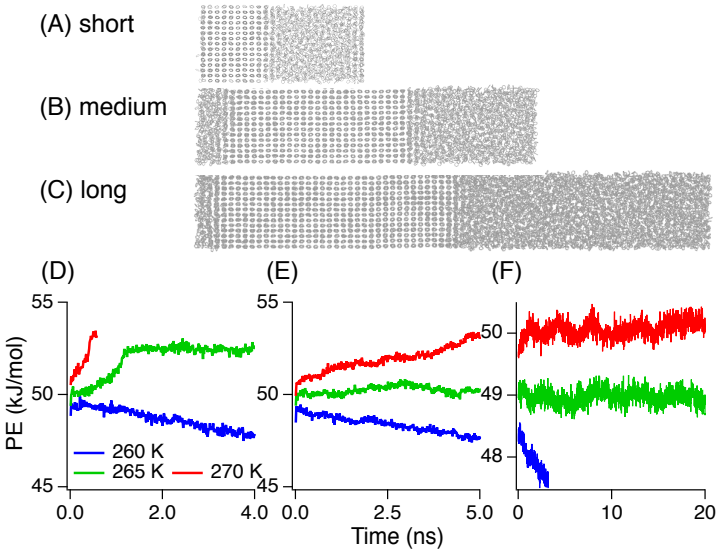


Figure 1. Estimation of T_m of benzene phase I in our computational model using the direct-coexistence method, performed for three different systems, (**A**) short, (**B**) medium, and (**C**) long. Initial configurations including liquid (right half) and solid (left half) phases, and time evolution of average potential energy (PE) per molecule in NpT-MD simulations at three temperatures (260, 265, and 270 K) for (**D**) short, (**E**) medium, and (**F**) long systems.

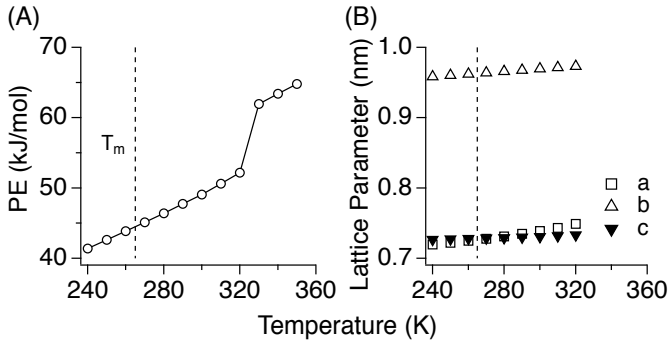


Figure 2. Temperature dependence of (**A**) average PE per molecule, and (**B**) lattice parameters of benzene crystal (a, b, and c). Error bars are smaller than the symbols in both the panels. Dashed black line indicates equilibrium melting temperature T_m.

3.2. Induction Time

We investigated the characteristics of melting dynamics in terms of induction (waiting) time. Below the superheating limit, there is a free-energy barrier between the crystal and liquid phases, and the system was observed to remain at a superheated crystal phase until a melting pathway can be obtained. We obtained 100 independent melting trajectories at 323 and 324 K by providing a different set of velocities to the initial configuration, equilibrated at 320 K. Figure 3A displays the time evolution of the potential energy per molecule for three typical melting trajectories obtained at 323 K. During the induction period, the potential energy fluctuates; however, its mean value does not change. The blue curve shows a small jump of potential energy before melting starts, which arises from a longevity

melting nucleus. However, this behavior was not observed in the remaining 199 melting trajectories. Thus, we did not give special weight to the jump. After several hundred ps, the ordered crystal structure spontaneously collapses with increasing potential energy. If there is a transient metastable state between the crystal and liquid phases, potential energy presents a stepwise change owing to the Ostwald step rule [54]. However, the homogeneous melting of benzene in the 200 melting trajectories observed in our study was always completed without any steps.

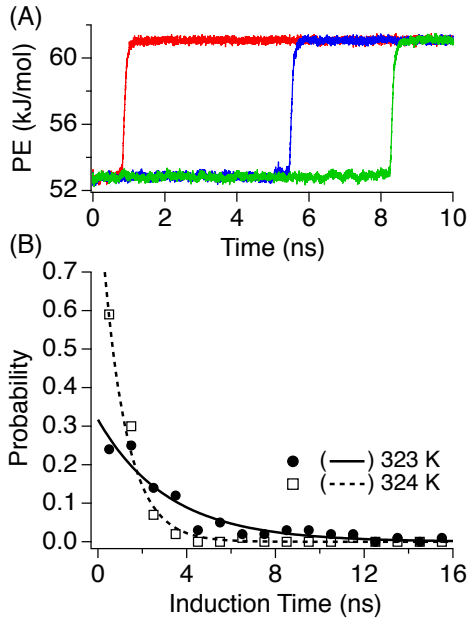


Figure 3. Induction time. (**A**) Time evolution of potential energy (PE) per molecule for the three melting trajectories obtained at 323 K; (**B**) probability distributions of induction times (τs) for melting at 323 and 324 K, where solid and dashed curves denote exponential functions $\tau_0^{-1}\exp(-\tau/\tau_0)$ fitted to the distributions.

To further confirm that the homogeneous melting of benzene is governed by a stochastic transition between two states, we investigate the statistics of induction time τ. If the phase transition is random between the initial and final states, and exhibits a short memory time with a constant probability of occurrence per unit time (τ_0^{-1}), the probability distribution of τ can be expressed by $\tau_0^{-1}\exp(-\tau/\tau_0)$; further, average τ is $\langle\tau\rangle = \tau_0$ [55]. In addition, nucleation rate J is estimated by $J = \tau_0^{-1}V^{-1}$, where V is the volume of the simulation box in the crystal state. However, if the transition is complicated, such as a multistep transition, the probability distribution of τ obeys a different function [56], and the computed values of τ_0 and $\langle\tau\rangle$ do not agree.

We define induction time τ as the time period from the beginning of the MD run at 323 K (or 324 K) to the instant at which the potential energy is midway between the mean values of the crystal and liquid phases. For example, the τ of the melting trajectories in Figure 3A is 0.9, 5.5, and 8.3 ns. Figure 3B depicts the probability distribution of τs at 323 and 324 K. We observed that the probability distribution can be fitted well using the aforementioned exponential function ($\tau_0^{-1}\exp(-\tau/\tau_0)$) at both temperatures even though distribution is strongly dependent on temperature. The estimated values of τ_0s agree well with the values of $\langle\tau\rangle$, which are directly computed from MD runs; it was observed that τ_0 = 3.2 ns and $\langle\tau\rangle$ = 3.4 ns at 323 K, and that τ_0 = 1.1 ns and $\langle\tau\rangle$ = 1.2 ns at 324 K. We also estimated the nucleation rate to be $J = 3.2 \times 10^{26}$ cm^{-3} s^{-1} at 323 K and 9.3×10^{26} cm^{-3} s^{-1} at 324 K. These results indicate that the homogeneous melting of benzene can be described by a classical two-state transition model [57], in which the metastable crystal phase stochastically transforms to the stable liquid phase.

3.3. Nucleation

Here, we investigate the spontaneous formation of liquid nucleus inside the crystal. To distinguish the disordered structure from the structure of the benzene crystal with a pseudo-FCC lattice, we computed averaged bond order parameter $\bar{q}_6$ for each benzene molecule using their centers of mass [58]. $\bar{q}_6$ captures local symmetry. Two benzene molecules are considered to be adjacent if the distance between their centers of mass is shorter than 0.69 nm, where the radial-distribution function of the crystal structures at 320 K exhibits a second minimum; further, the number of neighbors is 12 molecules. In Figure 4, we compare the probability distribution of $\bar{q}_6$ for structures of bulk crystal at 320 K and bulk liquid at 330 K. Benzene-crystal distribution has a peak at $\bar{q}_6$ = 0.49, which is the same as that for a perfect FCC crystal [58]. Further, there is no overlap between distributions. Therefore, $\bar{q}_6$ is expected to identify the disordered benzene structure that is formed in the crystal. Here, we define a benzene molecule as liquid if its $\bar{q}_6$ is less than 0.4.

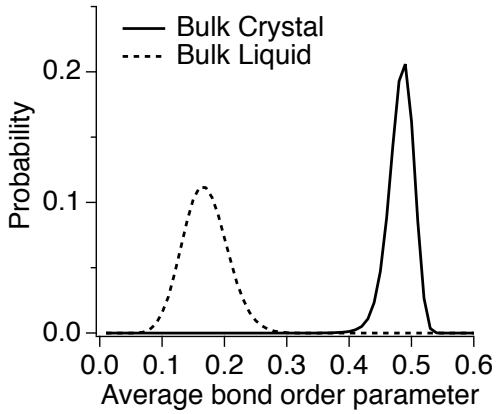


Figure 4. Probability distributions ofthe average bond order parameter $\bar{q}_6$ for a bulk crystal at 320 K and a bulk liquid at 330 K.

We focus on one of the typical melting trajectories at 323 K, where melting occurs after sufficient induction time. The analysed trajectory is the same as that of the green line in Figure 3A. Figure 5A presents the time evolution of the total number of liquid benzene molecules n_t and the largest cluster size n_c, where two benzene molecules are considered to form the same cluster if they are adjacent. In Figure 5A, the spikes in n_t and n_c demonstrate that the melting nucleus, which can be considered to be a defect if the size is small, repeatedly appears and disappears during induction time. At this temperature, liquid benzene always exists in the crystal, and average n_t and n_c before melting (<8.2 ns) were 16.1 and 8.4 molecules in our system (N = 7280), respectively. When n_t is small, there are clusters so that n_c and n_t are different (Figure 6A–C). When melting begins, one of them grows into the melting nucleus, and the remaining small clusters are subsequently merged into the largest (Figure 6D). Figure 6A–C shows that their birthplaces are not fixed at a specific position but randomly scattered in space. At approximately 8.25 ns, n_c is equal to more than 200 molecules; further, the melting nucleus grows rapidly and transforms to bulk liquid within 150 ps (the inset of Figure 5A). These results imply that critical nucleus size is likely to be smaller than 200 molecules, beyond which the melting process is shifted from nucleation to nucleus growth.

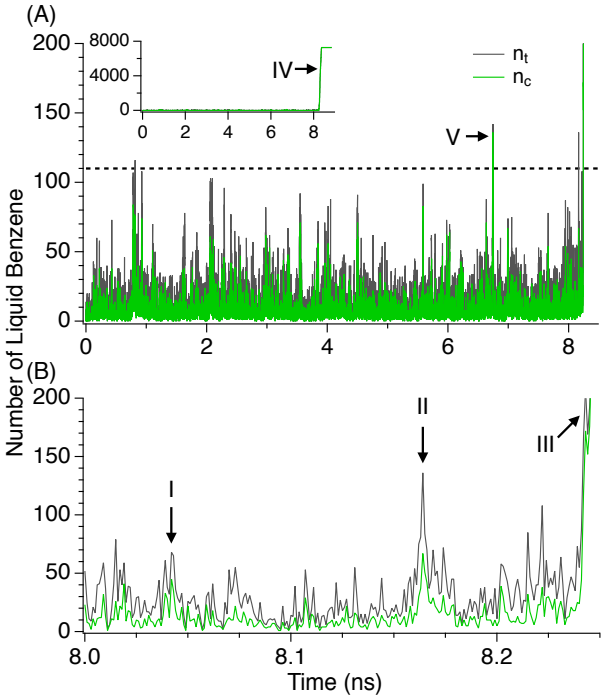


Figure 5. Time evolution of total number of liquid benzene molecules n_t and largest liquid cluster size n_c for (**A**) the whole induction time and (**B**) the short period just before melting occurs. Inset in (**A**) shows the entire melting process. Dashed line represents the size of critical nucleus n_c^* estimated by the seeding method (110 molecules).

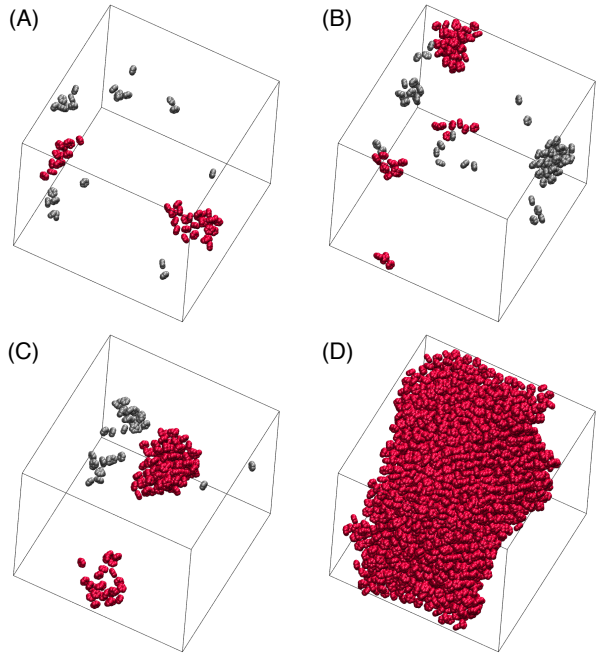


Figure 6. Snapshots of instantaneous structures at (**A**) 8.042, (**B**) 8.164, (**C**) 8.243, and (**D**) 8.303 ns, which correspond to the black arrows in Figure 5. Only liquid molecules are denoted. Largest cluster size n_c at these times was 45, 67, 172, and 4028 molecules, respectively, represented by red. Although the largest cluster (red) appears to be divided into parts, these parts are connected over the periodic boundary. The panels A–D correspond to Moments I–IV in Figure 5.

3.4. Critical Nucleus Size

To determine the critical nucleus size, we adopted the seeding approach [59,60]. A seed for a melting nucleus could be obtained from our melting trajectory. Further, 10 independent, 20 ps-long NpT-MD runs are initiated from the seed owing to the generation of different velocities. Figure 7A depicts the time evolution of n_c for a swarm of trajectories beginning from the melting nucleus of n_c = 172, corresponding to Structure C in Figure 6. The results denote that the melting nucleus grows in some trajectories, whereas it shrinks in other trajectories. The average value, $\langle n_c \rangle$, did not significantly change (see blue line in Figure 7A), thereby indicating that the system is close to the hill-top on the free-energy landscape. In comparison, the melting nucleus grows in the majority of the trajectories when the trajectory begins from the melting nucleus of n_c = 210 (Figure 7B). Here, the initial nucleus size is already greater than the critical nucleus size. Further, we quantified average growth speed $d\langle n_c \rangle / dt$ for an ensemble of seed nuclei ranging from n_c = 60 to 220, randomly sampled from the obtained melting MD trajectories. Figure 7C depicts that $d\langle n_c \rangle / dt$ is directly proportional to the initial n_c even though its large dispersion indicates that n_c is not the only order parameter defining the melting progress. The linear fit of the dataset shows critical nucleus size n_c^* with $d\langle n_c \rangle / dt = 0$ being approximately 110 molecules. This size is consistent with the observation that the fluctuation of n_c rarely results in more than 110 molecules during induction time (Figure 5A).

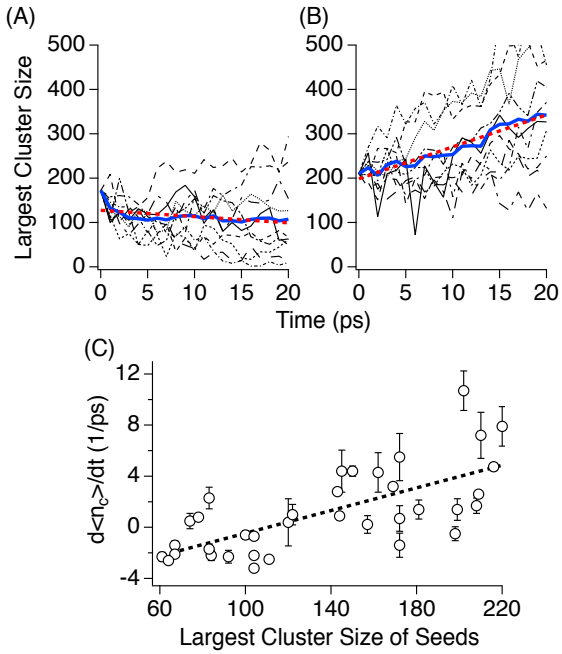


Figure 7. Time evolution of nuclei in 10 independent trajectories, beginning from (**A**) n_c = 172 and (**B**) 210. Initial seed in A corresponds to Snapshot C in Figure 6. Blue lines indicate average value $\langle n_c \rangle$. Red dashed lines are linear fits of $\langle n_c \rangle$, from which average growth speed $d\langle n_c \rangle / dt$ can be calculated. (**C**) Plot of $d\langle n_c \rangle / dt$ as a function of the initial n_c of the seeds. Further, black dashed line indicates linear fit.

3.5. Diffusive Motion

What is the key motion that is required for producing the critical melting nucleus? Studies on ice [20], metals [17,21–23], Lennard–Jones fluids [24–27] and colloids [9] denoted that the precursor for homogeneous melting is the diffusion of molecules, which is activated by defects or co-operative motion. These precursors promote the swapping of molecules and change their lattice sites while the whole crystal structure remains intact. Further, we compute the time evolution of mean square displacement (MSD) with respect to the initial configuration, $\langle |\mathbf{r}_i(t) - \mathbf{r}_i(0)|^2 \rangle$, where $\mathbf{r}_i(t)$ is the coordinate vector of the centre of mass for the ith molecule at time t; further, bracket $\langle \cdots \rangle$ denotes the

average over all molecules. Figure 8A depicts that MSD does not increase during induction time, which is in contrast to that observed in a Lennard–Jones crystal [27]. Furthermore, the projection against n_c demonstrates that MSD increases after n_c becomes larger than critical nucleus size n_c* (Figure 8B). These results indicate that large diffusive motions induced by defect migration or neighbor-molecule swapping do not contribute to the formation of the melting nucleus.

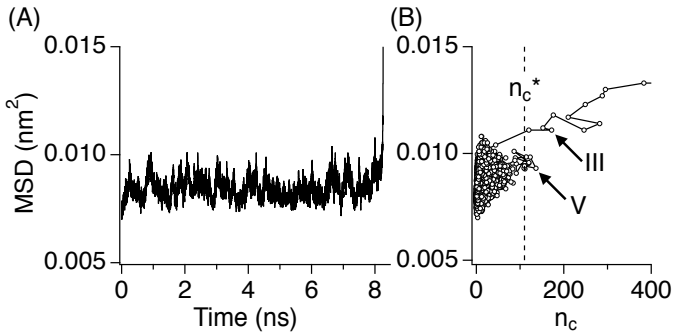


Figure 8. Mean square displacement (MSD), as computed for the same trajectory depicted in Figure 5, is plotted against (**A**) time and (**B**) largest cluster size n_c. In (**B**), the dashed line indicates critical nucleus size n_c^*, and black arrows indicate Moments III and V that correspond to those observed in Figure 5.

Furthermore, we compare two particular moments, III (t = 8.243 ns) and V (t = 6.740 ns), which are indicated by black arrows in Figure 8B. Although n_c values at both moments were larger than n_c^*, the melting nucleus did not grow after Moment V. Further, we can observe that the MSD at Moment V remained small, indicating that the distance from the perfect crystal on the conformational space was not sufficiently large. Indeed, the system repairs the disordered structure and the crystal structure is restored by thermal fluctuation (see Figure 5). The difference between Moments III and V indicates that the quality of the melting nucleus, in addition to n_c, should be taken into consideration for more accurately defining the melting progress.

3.6. Rotational Motion

We investigated the rotational motion of benzene crystal molecules. To characterize their orientation, we focused on two orthogonal unit vectors, vector **q** perpendicular to the molecular plane, and in-plane vector **u** that passes through two carbon atoms that are located on opposite sides of the molecule (Figure 9A). Vectors **q** and **u** denote the six- and twofold axes of the molecule, respectively. Figure 9B depicts self-reorientational correlation function (RCF) $\langle \mathbf{u}_i(t) \cdot \mathbf{u}_i(0) \rangle$ for vector **u** at 240, 280, and 320 K. All functions decay in the order of a few tens of picoseconds, and the rotation of **u** becomes faster with increasing T. We evaluated relaxation time τ_u by a fit of $\exp(-t/\tau_u)$; values of τ_u were 64, 22, and 9 ps at 240, 280, and 320 K, respectively. Even at the lowest temperature of 240 K ($<T_m$), relaxation time τ_u = 64 ps was considerably shorter than heating time (10 ns long MD run at each temperature). Further, we analyzed the rotational behavior of one molecule. In Figure 9C,D, time evolution of angle $\theta_u = \mathrm{acos}\{\mathbf{u}_i(t) \cdot \mathbf{u}_i(0)\}$ is plotted for a typical molecule at 240 and 320 K, respectively. The results depict that rotation occurs by discrete jumps between θ_u = 0, 60, 120, and 180 degrees, and the frequency of the jumps increases with T owing to larger thermal energy. We later depict that the relaxation of **q** is hundreds of times slower than that of **u**, so that the reorientation of **u** is considered independent from that of **q**, occurring around the sixfold axis (vector **q**). In such a case, the conformation of the benzene molecule is identical between θ_u = 0, 60, 120, and 180 degrees and does not distort the crystal structure. Because benzene molecules in a crystal frequently rotate around the sixfold axis, even at almost one hundred degrees lower than the homogeneous melting temperature, this motion is unlikely to influence the formation of the melting nucleus.

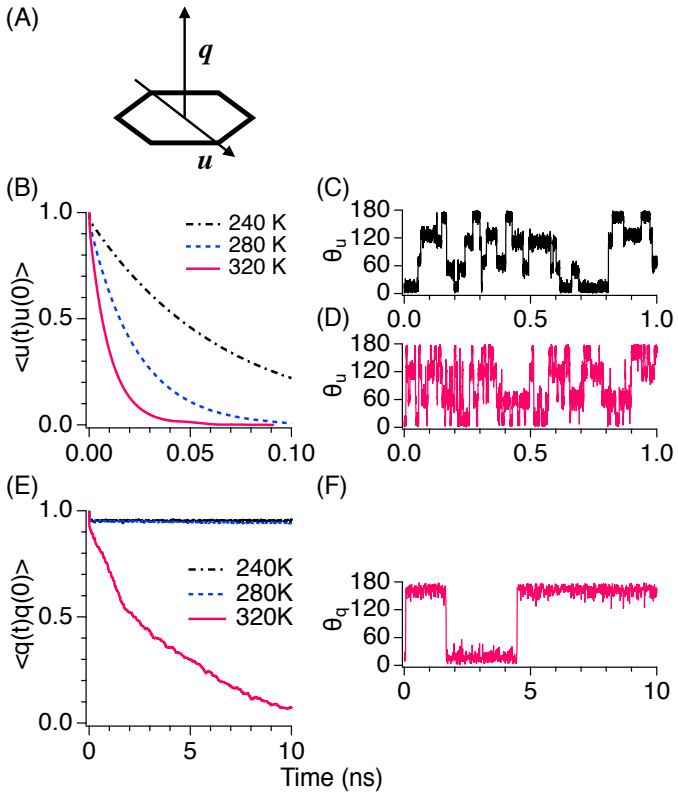


Figure 9. Analyses of rotational motions. (**A**) Illustration of two vectors **u** and **q** on a hexagonal benzene molecule. Reorientational correlation functions (RCFs) for vectors (**B**) **u** and (**E**) **q** at three temperatures. Time evolution of angles θ_u in the unit of degree at (**C**) 240 K and (**D**) 320 K, and (**F**) angle θ_q at 320 K, as computed for a typical benzene molecule.

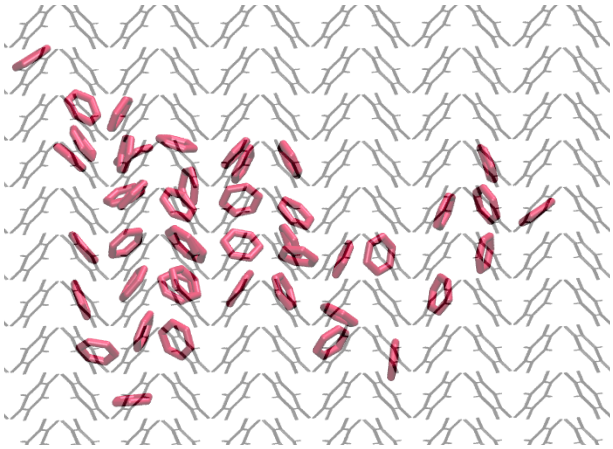


Figure 10. Projection of the largest cluster (thick red) observed at Time I on the crystal structure (thin black).

RCF analyses depict that the relaxation of **q** was significantly slower than that of **u** (Figure 9E). At 240 and 280 K, the RCF does not decrease over a period of 10 ns, indicating the reorientation of **q** is negligible. However, the RCF decays in the order of a few ns at 320 K, which is close to the homogeneous melting temperature. We monitored the time evolution of angle $\theta_q = \text{acos}\{\mathbf{q}_i(t) \cdot \mathbf{q}_i(0)\}$ for each benzene molecule. The angle changed only a few times in 10 ns at 320 K. Figure 9F denotes one of the typical examples. The change between θ_q = 0 and 180 degrees arises from the flipping motion of the molecule plane. If benzene molecules are completely flipped, the motion does not affect the crystal structure. However, we observed that benzene molecules sometimes fail to completely

flip, thereby inducing orientational disorder. The benzene molecule is not spherical; the unfavored orientation dislocates the surrounding molecules, and the resulting asymmetric structure is detected by order parameter $\bar{q}_6$. The overlap of the small melting nucleus, corresponding to Moment I in Figure 6, on the crystal structure is depicted in Figure 10. The snapshot clearly illustrates that the melting nucleus comprises orientational disorder, while the translational order of the centers of mass is maintained considerably well (we can observe the alignment along the vertical and horizontal directions). To further confirm the influence of the flipping motion on nucleation, we computed the average change of vector $\mathbf{q}$ at time t with respect to Δt=10 ps before; $\langle \Delta\theta_q(t) \rangle = \sum_i^N \mathrm{acos}\{\mathbf{q}_i(t) \cdot \mathbf{q}_i(t - \Delta t)\}/N$. Then, we found that the correlation coefficient between $\langle \Delta\theta_q(t) \rangle$ and the total number of liquid benzene n_t was 0.51 at the induction time, indicating moderate correlation. Along with the analyses for diffusional and rotational modes, we can conclude that the flipping motion that was activated near the melting temperature triggered the formation of the melting nucleus.

4. Summary

In this study, the molecular mechanism of the homogeneous melting of benzene phase I was investigated using MD simulations. Further, we intended to understand the manner in which a nonspherical apolar organic crystal with a well-packed structure generated internal disorder. We demonstrated that melting occurs stochastically in the benzene crystal, and that there was no transient state between them at the superheated temperature at which our simulations have been performed. While defect migration and neighboring-molecule swapping were not observed before melting began, benzene molecules began to explicitly diffuse when the melting nucleus became larger than the critical size. In comparison, we observed that the flipping rotational motion is important for the formation of critical melting nucleus because the nucleus exhibits orientational disorder. In addition to elucidating the homogeneous melting of benzene phase I, our study may serve as the basis for understanding the phase-transition dynamics of other polycyclic aromatic hydrocarbons (such as perylene [61,62]) that possess a complicated free-energy landscape, including metastable crystals.

Author Contributions: All of this work has been done by K.M.

Funding: This research was funded by JSPS KAKENHI grant number 15H05474 and URA funds in Shinshu University.

Acknowledgments: Most calculations were performed at the Research Center for Computational Science in Okazaki, Japan.

Conflicts of Interest: The authors declare no conflict of interest.

References

1. Lindemann, F.A. Ueber die berechnung molekularer eigenfrequenzen. *Z. Phys.* **1910**, *11*, 609–612.
2. Born, M. Thermodynamics of crystals and melting. *J. Chem. Phys.* **1939**, *7*, 591–603. [CrossRef]
3. Murata, K.I.; Asakawa, H.; Nagashima, K.; Furukawa, Y.; Sazaki, G. Thermodynamic origin of surface melting on ice crystals. *Proc. Natl. Acad. Sci. USA* **2016**, *113*, E6741–E6748. [CrossRef] [PubMed]
4. Li, B.; Wang, F.; Zhou, D.; Peng, Y.; Ni, R.; Han, Y. Modes of surface premelting in colloidal crystals composed of attractive particles. *Nature* **2016**, *531*, 485–488. [CrossRef] [PubMed]
5. Banhart, F.; Hernández, E.; Terrones, M. Extreme superheating and supercooling of encapsulated metals in fullerenelike shells. *Phys. Rev. Lett.* **2003**, *90*, 185502. [CrossRef] [PubMed]
6. Daeges, J.; Gleiter, H.; Perepezko, J.H. Superheating of metal crystals. *Phys. Lett. A* **1986**, *119*, 79–82. [CrossRef]
7. Herman, J.W.; Elsayed-Ali, H.E. Superheating of Pb(111). *Phys. Rev. Lett.* **1992**, *69*, 1228–1231. [CrossRef] [PubMed]
8. Siwick, B.J.; Dwyer, J.R.; Jordan, R.E.; Miller, R.J.D. An atomic-level view of melting using femtosecond electron diffraction. *Science* **2003**, *302*, 1382–1385. [CrossRef]
9. Wang, Z.; Wang, F.; Peng, Y.; Zheng, Z.; Han, Y. Imaging the homogeneous nucleation during the melting of superheated colloidal crystals. *Science* **2012**, *338*, 87–90. [CrossRef]

10. Wang, Z.; Wang, F.; Peng, Y.; Han, Y. Direct observation of liquid nucleus growth in homogeneous melting of colloidal crystals. *Nat. Commun.* **2015**, *6*, 6942. [CrossRef]
11. Mo, M.Z.; Chen, Z.; Li, R.K.; Dunning, M.; Witte, B.B.L.; Baldwin, J.K.; Fletcher, L.B.; Kim, J.B.; Ng, A.; Redmer, R.; et al. Heterogeneous to homogeneous melting transition visualized with ultrafast electron diffraction. *Science* **2018**, *360*, 1451–1455. [CrossRef] [PubMed]
12. Iglev, H.; Schmeisser, M.; Simeonidis, K.; Thaller, A.; Laubereau, A. Ultrafast superheating and melting of bulk ice. *Nature* **2006**, *439*, 183–186. [CrossRef] [PubMed]
13. Wang, F.; Zhou, D.; Han, Y. Melting of Colloidal Crystals. *Adv. Funct. Mater.* **2016**, *26*, 8903–8919. [CrossRef]
14. Wang, F.; Wang, Z.; Peng, Y.; Zheng, Z.; Han, Y. Homogeneous melting near the superheat limit of hard-sphere crystals. *Soft Matter* **2018**, *14*, 2447–2453. [CrossRef]
15. Liang, S.; Yi, L.; Liang, D. Molecular Insights into the Homogeneous Melting of Methane Hydrates. *J. Phys. Chem. C* **2014**, *118*, 28542–28547. [CrossRef]
16. Jin, Z.H.; Gumbsch, P.; Lu, K.; Ma, E. Melting mechanisms at the limit of superheating. *Phys. Rev. Lett.* **2001**, *87*, 055703. [CrossRef] [PubMed]
17. Samanta, A.; Tuckerman, M.E.; Yu, T.Q.; Weinan, E. Microscopic mechanisms of equilibrium melting of a solid. *Science* **2014**, *346*, 729–732. [CrossRef]
18. Grishina, N.; Buch, V. Structure and dynamics of orientational defects in ice I. *J. Chem. Phys.* **2004**, *120*, 5217–5225. [CrossRef]
19. Donadio, D.; Raiteri, P.; Parrinello, M. Topological Defects and Bulk Melting of Hexagonal Ice. *J. Phys. Chem. B* **2005**, *109*, 5421–5424. [CrossRef]
20. Mochizuki, K.; Matsumoto, M.; Ohmine, I. Defect pair separation as the controlling step in homogeneous ice melting. *Nature* **2013**, *498*, 350–354. [CrossRef]
21. Forsblom, M.; Grimvall, G. How superheated crystals melt. *Nat. Mater.* **2005**, *4*, 388–390. [CrossRef] [PubMed]
22. Forsblom, M.; Grimvall, G. Homogeneous melting of superheated crystals: Molecular dynamics simulations. *Phys. Rev. B* **2005**, *72*, 054107. [CrossRef]
23. Zhang, H.; Khalkhali, M.; Liu, Q.; Douglas, J.F. String-like cooperative motion in homogeneous melting. *J. Chem. Phys.* **2013**, *138*, 12A538. [CrossRef]
24. Delogu, F. Defect-mediated melting in superheated noble gas crystals. *J. Phys. Chem. B* **2005**, *109*, 20295–20302. [CrossRef] [PubMed]
25. Delogu, F. Cooperative dynamics and self-diffusion in superheated crystals. *J. Phys. Chem. B* **2005**, *109*, 15291–15296. [CrossRef] [PubMed]
26. Gómez, L.; Dobry, A.; Geuting, C.; Diep, H.T.; Burakovsky, L. Dislocation Lines as the Precursor of the Melting of Crystalline Solids Observed in Monte Carlo Simulations. *Phys. Rev. Lett.* **2003**, *90*, 095701. [CrossRef] [PubMed]
27. Bai, X.M.; Li, M. Ring-diffusion mediated homogeneous melting in the superheating regime. *Phys. Rev. B* **2008**, *77*, 609–13. [CrossRef]
28. Cahn, R.W. Melting from within. *Nature* **2001**, *413*, 582–583. [CrossRef]
29. Raiteri, P.; Martoňák, R.; Parrinello, M. Exploring Polymorphism: The Case of Benzene. *Angew. Chem. Int. Ed.* **2005**, *44*, 3769–3773. [CrossRef]
30. Chanyshev, A.D.; Litasov, K.D.; Rashchenko, S.V.; Sano-Furukawa, A.; Kagi, H.; Hattori, T.; Shatskiy, A.F.; Dymshits, A.M.; Sharygin, I.S.; Higo, Y. High-Pressure–High-Temperature Study of Benzene: Refined Crystal Structure and New Phase Diagram up to 8 GPa and 923 K. *Cryst. Growth Des.* **2018**, *18*, 3016–3026. [CrossRef]
31. Wen, X.D.; Hoffmann, R.; Ashcroft, N.W. Benzene under High Pressure: A Story of Molecular Crystals Transforming to Saturated Networks, with a Possible Intermediate Metallic Phase. *J. Am. Chem. Soc.* **2011**, *133*, 9023–9035. [CrossRef] [PubMed]
32. Headen, T.F.; Howard, C.A.; Skipper, N.T.; Wilkinson, M.A.; Bowron, D.T.; Soper, A.K. Structure of pi-pi interactions in aromatic liquids. *J. Am. Chem. Soc.* **2010**, *132*, 5735–5742. [CrossRef] [PubMed]
33. Yoshida, K.; Fukuyama, N.; Yamaguchi, T.; Hosokawa, S.; Uchiyama, H.; Tsutsui, S.; Baron, A.Q.R. Inelastic X-ray scattering on liquid benzene analyzed using a generalized Langevin equation. *Chem. Phys. Lett.* **2017**, *680*, 1–5. [CrossRef]

34. Nagasaka, M.; Yuzawa, H.; Mochizuki, K.; Rühl, E.; Kosugi, N. Temperature-Dependent Structural Changes in Liquid Benzene. *J. Phys. Chem. Lett.* **2018**, *9*, 5827–5832. [CrossRef] [PubMed]
35. Shah, M.; Santiso, E.E.; Trout, B.L. Computer simulations of homogeneous nucleation of benzene from the melt. *J. Phys. Chem. B* **2011**, *115*, 10400–10412. [CrossRef] [PubMed]
36. Tohji, K.; Murata, Y. X-Ray Diffraction Study of the Melting of Benzene. *Jpn. J. Appl. Phys.* **1982**, *21*, 1199–1204. [CrossRef]
37. Craven, C.J.; Hatton, P.D.; Howard, C.J.; Pawley, G.S. The structure and dynamics of solid benzene. I. A neutron powder diffraction study of deuterated benzene from 4 K to the melting point. *J. Chem. Phys.* **1993**, *98*, 8236–8243. [CrossRef]
38. MacKerell, A.D.; Bashford, D.; Bellott, M.; Dunbrack, R.L.; Evanseck, J.D.; Field, M.J.; Fischer, S.; Gao, J.; Guo, H.; Ha, S.; et al. All-atom empirical potential for molecular modeling and dynamics studies of proteins. *J. Phys. Chem. B* **1998**, *102*, 3586–3616. [CrossRef]
39. MacKerell, A.D.; Wiorkiewicz-Kuczera, J.; Karplus, M. An all-atom empirical energy function for the simulation of nucleic acids. *J. Am. Chem. Soc.* **1995**, *117*, 11946–11975. [CrossRef]
40. Nemkevich, A.; Bürgi, H.B.; Spackman, M.A.; Corry, B. Molecular dynamics simulations of structure and dynamics of organic molecular crystals. *Phys. Chem. Chem. Phys.* **2010**, *12*, 14916–14929. [CrossRef]
41. Tsuzuki, S.; Honda, K.; Uchimaru, T.; Mikami, M.; Tanabe, K. Origin of attraction and directionality of the pi/pi interaction: Model chemistry calculations of benzene dimer interaction. *J. Am. Chem. Soc.* **2002**, *124*, 104–112. [CrossRef] [PubMed]
42. Miller, E.D.; Jones, M.L.; Jankowski, E. Enhanced Computational Sampling of Perylene and Perylothiophene Packing with Rigid-Body Models *ACS Omega* **2017**, *2*, 353–362. [CrossRef]
43. Darden, T.; York, D.; Pedersen, L. Particle mesh Ewald: An N·log(N) method for Ewald sums in large systems. *J. Chem. Phys.* **1993**, *98*, 10089–10092. [CrossRef]
44. Berendsen, H.J.C.; van der Spoel, D.; van Drunen, R. GROMACS: A message-passing parallel molecular dynamics implementation. *Comput. Phys. Commun.* **1995**, *91*, 43–56. [CrossRef]
45. Hoover, W.G. Canonical dynamics: Equilibrium phase-space distributions. *Phys. Rev. A* **1985**, *31*, 1695–1697. [CrossRef]
46. Nosé, S. A molecular dynamics method for simulations in the canonical ensemble. *Mol. Phys.* **1984**, *52*, 255–268. [CrossRef]
47. Berendsen, H.J.C.; Postma, J.P.M.; van Gunsteren, W.F.; DiNola, A.; Haak, J.R. Molecular dynamics with coupling to an external bath. *J. Chem. Phys.* **1984**, *81*, 3684–3690. [CrossRef]
48. Bacon, G.; Curry, N.; Wilson, S. A crystalloraphic study of solid benzene by neutron diffraction. *Proc. R. Soc. Lond. A* **1964**, *279*, 98–110.
49. Cox, E.G.; Cruickshank, D.W.J.; Smith, J.A.S. The Crystal Structure of Benzene at -3Formula C. *Proc. R. Soc. Lond. Ser. A* **1958**, *247*, 1–21.
50. García Fernández, R.; Abascal, J.L.F.; Vega, C. The melting point of ice Ih for common water models calculated from direct coexistence of the solid-liquid interface. *J. Chem. Phys.* **2006**, *124*, 144506. [CrossRef]
51. Yagasaki, T.; Matsumoto, M.; Tanaka, H. Phase Diagrams of TIP4P/2005, SPC/E, and TIP5P Water at High Pressure. *J. Phys. Chem. B* **2018**, *122*, 7718–7725. [CrossRef]
52. Frenkel, D. Simulations: The dark side. *Eur. Phys. J. Plus* **2013**, *128*, 1208–21. [CrossRef]
53. Akella, J.; Kennedy, G.C. Phase Diagram of Benzene to 35 kbar. *J. Chem. Phys.* **1971**, *55*, 793–796. [CrossRef]
54. Mochizuki, K.; Himoto, K.; Matsumoto, M. Diversity of transition pathways in the course of crystallization into ice VII. *Phys. Chem. Chem. Phys.* **2014**, *16*, 16419–16425. [CrossRef] [PubMed]
55. Alfè, D.; Cazorla, C.; Gillan, M.J. The kinetics of homogeneous melting beyond the limit of superheating. *J. Chem. Phys.* **2011**, *135*, 024102–8. [CrossRef] [PubMed]
56. Knezic, D.; Zaccaro, J.; Myerson, A.S. Nucleation Induction Time in Levitated Droplets. *J. Phys. Chem. B* **2004**, *108*, 10672–10677. [CrossRef]
57. Erdemir, D.; Lee, A.Y.; Myerson, A.S. Nucleation of crystals from solution: Classical and two-step models. *Acc. Chem. Res.* **2009**, *42*, 621–629. [CrossRef]
58. Lechner, W.; Dellago, C. Accurate determination of crystal structures based on averaged local bond order parameters. *J. Chem. Phys.* **2008**, *129*, 114707. [CrossRef]
59. Knott, B.C.; Molinero, V.; Doherty, M.F.; Peters, B. Homogeneous Nucleation of Methane Hydrates: Unrealistic under Realistic Conditions. *J. Am. Chem. Soc.* **2012**, *134*, 19544–19547. [CrossRef]

60. Zimmermann, N.E.R.; Vorselaars, B.; Quigley, D.; Peters, B. Nucleation of NaCl from Aqueous Solution: Critical Sizes, Ion-Attachment Kinetics, and Rates. *J. Am. Chem. Soc.* **2015**, *137*, 13352–13361. [CrossRef]
61. Yago, T.; Tamaki, Y.; Furube, A.; Katoh, R. Growth of β-Perylene Crystal. *Chem. Lett.* **2007**, *36*, 370–371. [CrossRef]
62. Ito, F.; Kogasaka, Y.; Yamamoto, K. Fluorescence spectral changes of perylene in polymer matrices during the solvent evaporation process. *J. Phys. Chem. B* **2013**, *117*, 3675–3681. [CrossRef] [PubMed]



© 2019 by the author. Licensee MDPI, Basel, Switzerland. This article is an open access article distributed under the terms and conditions of the Creative Commons Attribution (CC BY) license (http://creativecommons.org/licenses/by/4.0/).